6

Computation of the Complex Impedance of a Cylindrical Conductor in an Ideal Two-Probe Configuration

V. Siva Kumar G. Kelekanjeri and Rosario A. Gerhardt
Georgia Institute of Technology
USA

1. Introduction

Impedance spectroscopy is an alternating current technique that can be used to probe materials or devices at length scales ranging from the atomic to macroscopic dimensions. Since its first application to solid state materials (Bauerle 1969), it has been used to characterize the electrical response of ionic electrolytes, ferroelectrics, intrinsic conducting polymers, ceramic and polymer matrix composites and biomaterials to name a few (Gerhardt 2005). The technique is based on probing the sample using an ac signal over a wide range of frequencies and studying the polarization phenomena associated with the electrical response. It is ideally suited for studying specimens where there is good electrical contrast at interfaces, either because of different constituent materials or because of space charge formation or dissipation. Impedance spectroscopy has recently been applied to nickel-base superalloys (Zou, Makram et al. 2002; Kelekanjeri[a] and Gerhardt 2006). These metallic alloys contain heterogeneities ranging in size from nanometers to micrometers and the measured impedance response shows interesting dependencies. As a first approximation, for the computations presented in this chapter, the heterogeneous material medium is regarded as a continuum with a uniform conductivity on a macro scale. This treatment is justified because the size of the microstructural heterogeneities is extremely small in relation to the measurement contact area. The problem dealt with here pertains to the specific case wherein circular electrodes are placed on opposite sides of a cylindrical specimen.

There are a few cases in the literature, where closed-form solutions in the frequency domain are available for problems similar to the current one. For example, Ney (Costache and Ney 1988; Ney 1991) derived a closed-form solution for the electric field distribution in a solid non-perfectly conducting flat ground plane as a result of electromagnetic interference. The derivation accounted for constriction effect as a result of confinement of current lines near the contact points and skin-effect due to finite conductivity of the ground plane. Bowler (Bowler[a] 2004) presented closed-form analytical expressions for the electric field distribution in a conducting half-space region due to alternating current injected at the surface. The analytical formulation was conducted in terms of a single, transverse magnetic potential in cylindrical coordinates and the solution was obtained by the use of the Hankel transform. In another publication, Bowler presented closed-form analytical expressions for the electric

field inside and outside a metal plate due to alternating current injected at the surface (Bowler[b] 2004). Current was injected and extracted via two separate wires, which were oriented normal to the surface of the plate. The problem was treated in two separate cylindrical co-ordinate systems where each wire was considered as the symmetry axis for the respective system (Bowler[b] 2004).

The derivation presented here addresses the specific problem of obtaining the electric field distribution inside a cylindrical metallic specimen due to current injection and extraction via oppositely placed electrode contacts (Kelekanjeri and Gerhardt 2007). Therefore, the problem while similar to the literature references cited above, corresponds to a distinctly different situation. This chapter also contains a description of the analytical treatment needed for computing the complex impedance response under the same conditions. All formulations are supported by independent finite-element (FE) validation using FEMLAB 3.1 (now COMSOL Multiphysics).

2. Problem description

A two-probe impedance measurement relies on the application of an ac signal across a specimen placed in between the source and the sink electrodes. The problem dealt with here considers the case where the electrodes are placed on the circular faces of the specimen and share the same axis of symmetry (see Fig. 1(a)). The measurement in essence can be treated as current injection into the specimen at the source electrode and current extraction at the sink electrode. In the actual measurement; however, the current is measured upon the application of a voltage.

An analytical formulation of this problem is developed by using Maxwell's equations for conductors (Hallen 1962; Cottingham and Greenwood 1991) and closed form analytical expressions for the resultant electric field distribution are derived in terms of Bessel series (www.mathworld.com; Gray and Mathews 1952; Abramowitz and Stegun 1964; Kreyszig 1994; Weber and Arfken 2004). The electric field distributions are then converted to the relevant impedance parameters. Additionally, finite element solutions for the electric field distributions and the impedance parameters are also presented in order to validate the derived analytical solutions. The Electromagnetics Module of FEMLAB package (COMSOL AB[a] 2004) is used to layout the finite element model. The finite element problem is formulated as a time-harmonic quasistatic application in the Meridional Currents/Potentials mode in terms of magnetic and electric potentials. The electric fields are ultimately obtained in terms of derivatives of magnetic and electric potentials. The solution obtained for the fields is subsequently used in computing an impedance spectrum of the specimen for the prescribed measurement configuration.

More specifically, the problem can be treated as the injection of an alternating current $I_o exp(-j\omega t)$ of angular frequency ω into a cylindrical metallic disk specimen, via a source electrode and extraction by means of a sink electrode (Kelekanjeri and Gerhardt 2007). The electrodes are modeled as perfect infinitesimally thick contacts of radius r_c contacting the specimen of radius r_o ($r_o >> r_c$) and thickness t_o ($t_o < r_o$) as shown in Fig. 1(a). The contact electrodes and the specimen are both axi-symmetric. The injected current at the source electrode, is assumed to be along the z direction. Due to a discrepancy between the size of the electrode contact and the specimen radius, there will be radial spreading of current flow lines within the specimen as shown in Fig. 1(b). This phenomenon, referred to as striction

effect or constriction (Costache and Ney 1988; Ney 1991), is where convergence or divergence of current flow lines occurs. A second effect is that of current flow confined to the surface of a conductor at high frequencies, an effect generally known as the skin-effect (Casimir and Ubbink 1967; Giacoletto 1996). As a consequence of the above two electrodynamic effects, there will be electric fields along both axial (*z)* and radial (*r)* directions (E_z and E_r) within the specimen, but, there will be no electric field in the tangential (φ) direction. The modeling measurement configuration (*r-z* plane), illustrating the skin and the constriction effects, is shown in Fig. 1(b). Since symmetry also exists about the *z* axis, the modeling space can further be condensed to one half of the *r-z* plane from $r = 0$ to $r = r_o$.

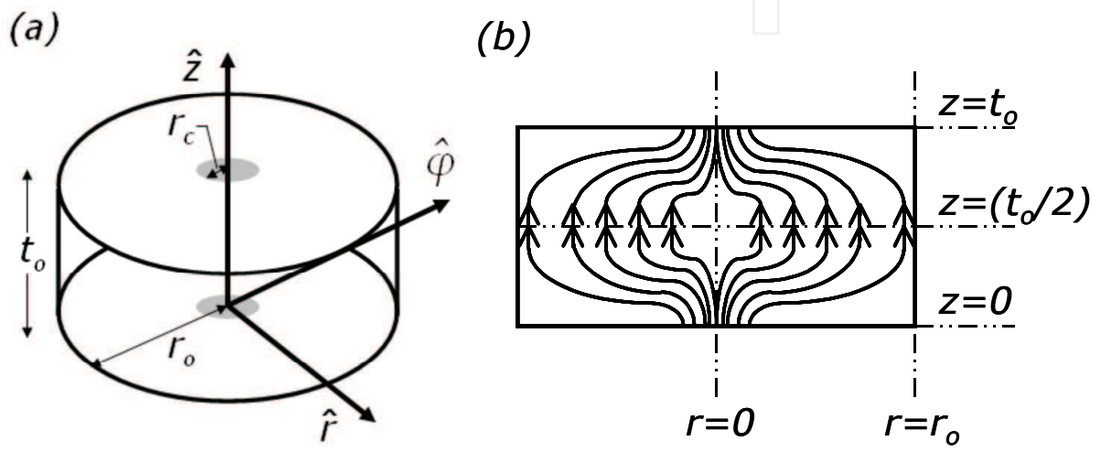

Figure 1. (a) Schematic illustrating the measurement geometry comprising of the specimen with coaxially placed electrodes (shown in gray shade) in a cylindrical co-ordinate system. The illustration in (b) shows the current flow contour incorporating both skin and constriction effects inside the specimen (*r-z* cross-section). The extent of radial spreading is enhanced with increasing frequency.

3. Analytical approach

3.1 Formulation and generic solution

The analytical solution for the electric field distribution (of angular frequency ω) inside the specimen (of uniform conductivity-σ and magnetic permeability-μ) is obtained by solving the following second order partial differential equation (PDE) (Ney 1991; Giacoletto 1996):

$$\overline{\nabla}^2 \overline{E} = \mu\sigma\left(\frac{\partial \overline{E}}{\partial t}\right) = j\omega\mu\sigma\overline{E} \tag{1}$$

Two independent partial differential equations in E_z and E_r may be written upon expanding the vector Laplacian (www.mathworld.com) using cylindrical co-ordinates as follows:

$$\frac{\partial^2 E_r}{\partial r^2} + \frac{\partial^2 E_r}{\partial z^2} + \frac{1}{r}\frac{\partial E_r}{\partial r} - \frac{E_r}{r^2} = j\omega\mu\sigma E_r \tag{2}$$

$$\frac{\partial^2 E_z}{\partial r^2}+\frac{\partial^2 E_z}{\partial z^2}+\frac{1}{r}\frac{\partial E_z}{\partial r}=j\omega\mu\sigma E_z \tag{3}$$

The general solutions for $E_r(r,z)$ and $E_z(r,z)$ for above PDE's may be expressed as follows:

$$E_r(r,z)=\left(C_5' e^{-\xi_1 z}+C_6' e^{\xi_1 z}\right)J_1(\lambda_1 r) \tag{4}$$

$$E_z(r,z)=\left(C_7' e^{-\xi_2 z}+C_8' e^{\xi_2 z}\right)J_o(\lambda_2 r) \tag{5}$$

where C_l' (l = 5,6,7 and 8) are the modified coefficients resulting from grouping the radial and axial solutions together.

3.2 Boundary conditions

The electric field distribution within the specimen is determined completely upon knowledge of the constants in the electric field expressions in equations (4) and (5). Examining the boundary conditions governing the two-probe impedance measurement problem is necessary to obtain the constants (Kelekanjeri and Gerhardt 2007):

a. Source and sink conditions:

$$\left(E_z\right)_{z=0,t_o}=\frac{I_o}{\pi {r_c}^2\sigma} \qquad \left(0\le r\le r_c\right) \tag{6}$$

$$=0 \qquad \left(r_c<r\le r_o\right)$$

$$\left(\frac{\partial E_z}{\partial r}\right)_{z=0,t_o}=-\frac{I_o}{\pi {r_c}^2\sigma}\delta(r_c-r) \tag{7}$$

b. Limiting normal current on curved boundary:

$$\left(E_r\right)_{r=r_o}=0\ ,\ \forall z \tag{8}$$

c. Conservation of current (I_o) via Ampere's law (Hallen 1962; Cottingham and Greenwood 1991):

$$\oint_c H_\varphi(r)_{r=r_o}\, r_o d\varphi = I_o \tag{9}$$

where H_φ is the magnetic field in the azimuthal (φ) direction, expressed in terms of the electric field components (E_r and E_z) as follows: (Hallen 1962; Cottingham and Greenwood 1991; Kelekanjeri and Gerhardt 2007):

$$H_\varphi(r,z)=\frac{1}{j\omega\mu}\left(\frac{\partial E_z}{\partial r}-\frac{\partial E_r}{\partial z}\right) \tag{10}$$

3.3 Determination of unique solution for electric field distribution

Applying the limiting current boundary condition imposed on $E_r(r,z)$, listed in equation (8), we obtain $J_1(\lambda_1 r)\big|_{r=r_o} = 0$ for a non-trivial solution. This equation has infinite roots (Kreyszig 1994; Weber and Arfken 2004), given by- $\lambda_{1i} = \frac{\beta_{1i}}{r_o}(i = 1,2,3...)$, where β_{1i} is a root of $J_1(x)$. Therefore, using the principle of superposition $E_r(r,z)$ may be rewritten as:

$$E_r(r,z) = \sum_m \left(C'_{5m} e^{-\xi_{1m} z} + C'_{6m} e^{\xi_{1m} z}\right) J_1(\lambda_{1m} r) \tag{11}$$

Next, the total current condition given by Ampere's law in equation (9) yields:

$$2\pi r_o H_\varphi(r,z)\big|_{r=r_o} = I_o \tag{12}$$

Substituting for $H_\varphi(r,z)$ from equation (10), we have:

$$\left(\frac{\partial E_z}{\partial r}\right)_{(r_o,z)} = \frac{j\omega\mu}{2\pi r_o} I_o \tag{13}$$

Since, the right hand side (RHS) term in the above equation is a constant, $E_z(r,z)$ must contain at least one term that is just a function of r and independent of z. Therefore, the expression for $E_z(r,z)$ may be modified as:

$$E_z(r,z) = f(r) + \left(C'_7 e^{-\xi_2 z} + C'_8 e^{\xi_2 z}\right) J_o(\lambda_2 r) \tag{14}$$

Substituting this new expression for $E_z(r,z)$ in equation (13), it is seen that only $f(r)$ contributes to total current and therefore $\left(\frac{\partial J_o(\lambda_2 r)}{\partial r}\right) = 0$. A non-trivial solution to this condition (see Appendix) is given by $\lambda_{2m} = \frac{\beta_{1m}}{r_o}(m = 1,2,3...)$, where β_{1m} is a root of $J_1(x)$. Thus the set of λ_i's and ξ_i's in the electric field expressions for $E_r(r,z)$ and $E_z(r,z)$ are determined as $\lambda_{1m} = \lambda_{2m} = \frac{\beta_{1m}}{r_o}$ and $\xi_{1m}{}^2 = \xi_{2m}{}^2 = \gamma^2 + \lambda_{1m}{}^2$. Applying the principle of superposition, the expression for $E_z(r,z)$ becomes:

$$E_z(r,z) = f(r) + \sum_m \left(C'_{7m} e^{-\xi_{1m} z} + C'_{8m} e^{\xi_{1m} z}\right) J_o(\lambda_{1m} r) \tag{15}$$

3.3.1 Problem symmetry

The pre-exponential coefficients - C'_i's that are left to be determined for a unique solution of the electric fields- $E_r(r,z)$ and $E_z(r,z)$ may be reduced in number by exploiting the symmetry of the problem. As mentioned previously, the problem geometry is both rotationally symmetric and axi-symmetric (about z axis). In addition, there is symmetry

about $z=\left(\frac{t_o}{2}\right)$ because the source and sink electrodes are placed on opposite circular faces of the specimen and centered about the z axis. A schematic illustrating the symmetric current flow contour incorporating constriction and skin effects is shown in Fig. 1(b). It is evident from the illustration that $E_z(r,z)$ is symmetric about $z=\left(\frac{t_o}{2}\right)$, whereas, $E_r(r,z)$ is anti-symmetric. Thus, we can write the following conditions:

$$E_r(r,z) = -E_r(r,t_o - z) \tag{16}$$

$$E_z(r,z) = E_z(r,t_o - z) \tag{17}$$

Using these conditions, the electric field expressions $E_r(r,z)$ and $E_z(r,z)$ may be modified by eliminating the constants- C'_{6m} and C'_{8m} as follows:

$$E_r(r,z) = \sum_m C'_{5m}\left(e^{-\xi_{1m}z} - e^{-\xi_{1m}(t_o - z)}\right)J_1(\lambda_{1m}r) \tag{18}$$

$$E_z(r,z) = f(r) + \sum_m C'_{7m}\left(e^{-\xi_{1m}z} + e^{-\xi_{1m}(t_o - z)}\right)J_o(\lambda_{1m}r) \tag{19}$$

3.3.2 Validation of 1-D skin-effect solution for f(r)

Consider the case of alternating current ($I_o exp(-j\omega t)$) flow through an infinitely long thin cylindrical wire along the z direction. In this case, the electric field distribution is governed only by skin-effect, which is given as (Giacoletto 1996):

$$E_z(r) = aJ_o(\kappa r) \tag{20}$$

where $a=\frac{\kappa I_o}{2\pi\sigma r_o J_1(\kappa r_o)}$ and $\kappa^2 = -j\omega\mu\sigma = -\gamma^2$.

Let us assume this solution for *f(r)* in the expression for $E_z(r,z)$ in equation (19). This assumption will be justified in the following by testing for the total current condition listed in equation (13). By virtue of this assumption, the expression for $E_z(r,z)$ now becomes:

$$E_z(r,z) = aJ_o(\kappa r) + \sum_m C'_{7m}\left(e^{-\xi_{1m}z} + e^{-\xi_{1m}(t_o - z)}\right)J_o(\lambda_{1m}r) \tag{21}$$

Substituting this expression for $E_z(r,z)$ in equation (13) (see Appendix for derivative of $J_o(x)$),

$$\left(\frac{\partial E_z}{\partial r}\right)_{(r_o,z)} = -\kappa a J_1(\kappa r_o) + \sum_m C'_{7m}\left(e^{-\xi_{1m}z} + e^{-\xi_{1m}(t_o - z)}\right)\left(-\lambda_{1m}J_1(\lambda_{1m}r_o)\right) = \frac{-\kappa^2 I_o}{2\pi\sigma r_o} = \frac{j\omega\mu}{2\pi r_o}I_o \tag{22}$$

The summation term vanishes as $J_1(\lambda_{1m}r_o) = J_1(\beta_{1m}) = 0$. The result is identical to the RHS of equation (13). Therefore, the starting assumption for *f(r)* is justified and the modified solution for $E_z(r,z)$ given in equation (21) stands correct. The first term in the expression

for $E_z(r,z)$ accounts for the skin-effect and the summation signifies the contribution from current constriction at the contacts.

The pre-exponential coefficient C'_{7m} may be determined by evaluating the integral $\int_0^{r_o}\left(\frac{\partial E_z}{\partial r}\right)_{z=0} J_1(\lambda_{1p}r)rdr$ using the source condition (equation (7)) and alternately using the expression for $E_z(r,z)$ in equation (21). The final answer is listed below:

$$C'_{7m}=\frac{\left\{\frac{I_o J_1(\lambda_{1p}r_c)}{\pi r_c \sigma}\right\}-\left\{\frac{\kappa a r_o}{\left(\kappa^2-{\lambda_{1p}}^2\right)}\left[\kappa J_2(\kappa r_o)J_1(\lambda_{1p}r_o)-\lambda_{1p}J_1(\kappa r_o)J_2(\lambda_{1p}r_o)\right]\right\}}{\left\{\frac{{\lambda_{1p}}{r_o}^2\left[J_2\left(\beta_{1p}\right)\right]^2\left(1+e^{-\xi_{1p}t_o}\right)}{2}\right\}} \tag{23}$$

The second coefficient C'_{5m} appearing in the expression for $E_r(r,z)$ may be determined by making use of Faraday's law (Cottingham and Greenwood 1991) as follows:

$$\overline{\nabla}\mathrm{x}\overline{\mathrm{H}}=\sigma\overline{\mathrm{E}}\Rightarrow-\left(\frac{\partial H_\varphi}{\partial z}\right)\hat{r}+\left(\frac{\partial H_\varphi}{\partial r}\right)\hat{z}=\sigma E_r\hat{r}+\sigma E_z\hat{z} \tag{24}$$

By substituting for H_φ from equation (10) and then comparing the r component on both sides of the equation, we have:

$$\left(\frac{\partial^2 E_z}{\partial z\partial r}-\frac{\partial^2 E_r}{\partial {z}^2}\right)=-j\omega\mu\sigma E_r \tag{25}$$

The coefficient C'_{5m} may be solved for by substituting the expressions for $E_r(r,z)$ and $E_z(r,z)$ in the above equation. The final answer is given as follows:

$$C'_{5m}=\frac{C'_{7m}\lambda_{1m}\xi_{1m}}{{\xi_{1m}}^2-j\omega\mu\sigma} \tag{26}$$

This completes the determination of the electric field distribution (described by equations (18) and (21)) inside a cylindrical disk shaped conductor for a two-probe impedance measurement.

3.3.3 Semi-infinite solution

Consider the case when the cylinder is infinitely long in the thickness (z) direction. The electric field distribution in this case can be obtained as a corollary to the derivation presented thus far. All the boundary conditions listed earlier are equally valid here. Therefore, the approach for obtaining the final solution is similar to the one presented for the disk problem. However, the only major difference between the solutions is that, terms involving $e^{+\xi_i z}$ are excluded from z-solutions for the present case. This essentially means

that the probability of a wave rebounding from the opposite boundary is negligible, which is a good approximation for large values of t_o.

The expressions for the axial and radial electric fields can then be written as follows (Kelekanjeri and Gerhardt 2007):

$$E_r(r,z) = \sum_m C'_{8m} e^{-\xi_{1m} z} J_1(\lambda_{1m} r) \tag{27}$$

$$E_z(r,z) = aJ_o(\kappa r) + \sum_m C'_{9m} e^{-\xi_{1m} z} J_o(\lambda_{1m} r) \tag{28}$$

The coefficients C'_{8m} and C'_{9m} may be solved for in a similar manner as shown for the disk solution. The above expressions are only valid from $z = 0$ to $\left(\frac{t_o}{2}\right)$; the solution for the other half of the cylinder is readily obtained by using the symmetry conditions listed in equations (16) and (17). Therefore, this problem will hereafter be referred to as the 'semi-infinite' case.

4. Finite element approach

The closed-form analytical expressions for the electric field distribution presented in the previous section were validated independently using a finite element solution obtained using the Electromagnetics Module of FEMLAB package (COMSOL AB[a] 2004). Modeling was conducted in the Meridional Currents/Potentials mode, which ensured rotational symmetry as well as symmetry about the *z* axis. The latter enforces that the radial current density and the gradient in the axial current density are both zero on the *z* axis, i.e. $J_r\big|_{r=0} = 0$ and $\left(\frac{\partial J_z}{\partial r}\right)\Big|_{r=0} = 0$ (COMSOL AB[a] 2004). The finite element model was formulated as a time-harmonic quasistatic problem in terms of magnetic ($\overline{A}$) and electric (V) potentials. The modeling geometry consists of one-half of *r-z* cross-section of the specimen (boundary 1 shows axial symmetry), which has been divided into sub-domains I and II as shown in Fig. 2. Boundaries-2 and 3 correspond to the source and sink electrode contacts respectively, where a constant current density is specified. The electric and magnetic fields are forced to be continuous across the vertical boundary (boundary-4) at $r = r_c$. Electric and magnetic insulation is specified at boundaries-5, 6 and 7. A Direct UMFPACK linear stationary solver (COMSOL AB[b] 2004) was used for obtaining the solution of the dependent variables, viz. the vector magnetic potential ($\overline{A}$) and the electric potential (V), for the following PDE (COMSOL AB[a] 2004):

$$\left(j\omega\sigma - \omega^2 \varepsilon_o \varepsilon_r\right)\overline{A} + \overline{\nabla} \mathrm{x}\left(\frac{\overline{\nabla} \mathrm{x} \overline{A}}{\mu_o \mu_r}\right) - \sigma \overline{\mathrm{v}} \mathrm{x}\left(\overline{\nabla} \mathrm{x} \overline{A}\right) + \left(\sigma + j\omega\varepsilon_o \varepsilon_r\right)\nabla V - \overline{J}^e = 0 \tag{29}$$

In the above equation, ε_o and ε_r refer to the absolute and relative permittivity and μ_o and μ_r refer to the absolute and relative magnetic permeability respectively. Subsequently, the electric and magnetic fields are obtained as:

$$\overline{E} = -\nabla V - \frac{\partial \overline{A}}{\partial t} \text{ and} \tag{30}$$

$$\overline{B} = \overline{\nabla} \mathrm{x} \overline{A} \tag{31}$$

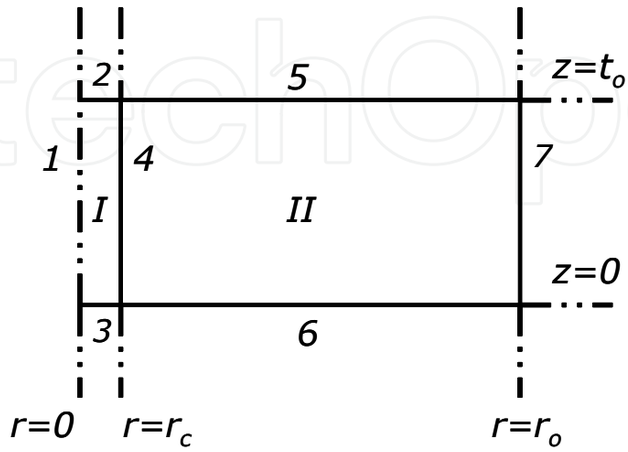

Figure 2. Illustration of the problem geometry (*r-z* cross-section) detailing the various sub-domains and boundaries as modeled in FEMLAB. Sub-domains I and II are parts of the complete specimen and are differentiated in order to indicate the electrode contacts on boundaries ($z=0$ and $z=t_o$) of sub-domain I. Sub-domain boundaries are numbered using Arabic numerals

5. Simulation results and discussion

In the first part of this section, a comparison between the electric field profiles (E_z and E_r) obtained via analytical and finite element simulations is presented. The two electrodynamic effects pertinent here, viz. the constriction and skin effects are discussed in detail based on the electric field profiles. Subsequently, the effects of varying one or more geometric parameters on the electric field profiles are studied systematically. Finally, the concept of a limiting thickness $t_{o,lim}$ is discussed, which is useful in ascertaining the applicability of the disk and semi-infinite analytical solutions for a given geometric configuration.

5.1 Electric field profiles

The following set of material properties and geometric parameters is used for computing the electric field profiles: σ =8.34 x 10^5 S/m, μ_r=1.004, r_o=5mm, r_c=0.5mm and t_o=2mm. An amplitude of I_o =50mA is assumed for the alternating current. A total of 53288 elements and 3126 boundary elements corresponding to a simulation space of 5x2sq.mm were used for finite element simulations. Figure 3 shows a comparison between the analytical and FEMLAB solutions as cross-section plots of the axial (E_z) and radial (E_r) electric field profiles at $z = \frac{t_o}{6}$ and a frequency of 1 MHz (Kelekanjeri[b] and Gerhardt 2006). It is clear from these plots that the analytical and FEMLAB solutions are in excellent agreement with

each other. Figure 4 shows surface plots of the axial field (E_z) at frequencies of 0.1 MHz ((a) & (c)) and 1 MHz, ((b) & (d)) obtained from the FEMLAB solution. The scale has been adjusted to emphasize the constriction behavior in 4(a) & 4(b) and the skin-effect behavior in 4(c) & 4(d). The symmetry of the field distribution about $z = \frac{t_o}{2}$ is clear from all the surface plots. It is seen from Figs. 4(a) and 4(b) that the field is concentrated near the electrode contacts, which is due to the constriction effect. The constriction effect in essence signifies the extent of radial spreading of the current. That this is the case, may be seen from Fig. 3(b), where the radial field $E_r(r,z)$ is a maximum at $r = r_c$, where the contacts terminate. Further away from the electrode contacts, the field decays rapidly along both z and r directions, as seen from the surface plots. The decay in E_z along the radial direction from $r = 0$ to $r = r_o$, may also be seen in the cross-section plot in Fig. 3(a), as the initial drop-off. This is due to progressive attenuation of the signal as it propagates within the medium. Increasing the frequency has the effect of enhancing the rate of field decay in the constriction region, as seen from the surface plots 4(a) and 4(b). The surface plots in Figs. 4(c) and 4(d) emphasize the skin-effect behavior at large values of r by using an altered scale. The surface plot in Fig. 4(d) clearly demonstrates that after the constriction drop-off, the field starts to rise near the end regions of the disk. This late rise in the field, as r approaches r_o, is also seen in the plot of E_z vs. r in Fig. 3(a). This behavior is due to the skin-effect, which forces the current to propagate closer to the surface, resulting in higher fields near the surface (Casimir and Ubbink 1967; Giacoletto 1996). The extent of rise is greater, the higher the frequency, as shown by the surface plots 4(c) and 4(d) at frequencies of 0.1 and 1MHz respectively. Thus at high frequencies, both the constriction and skin effects in combination determine the overall field distribution, whereas, constriction is the only dominant effect at low frequencies.

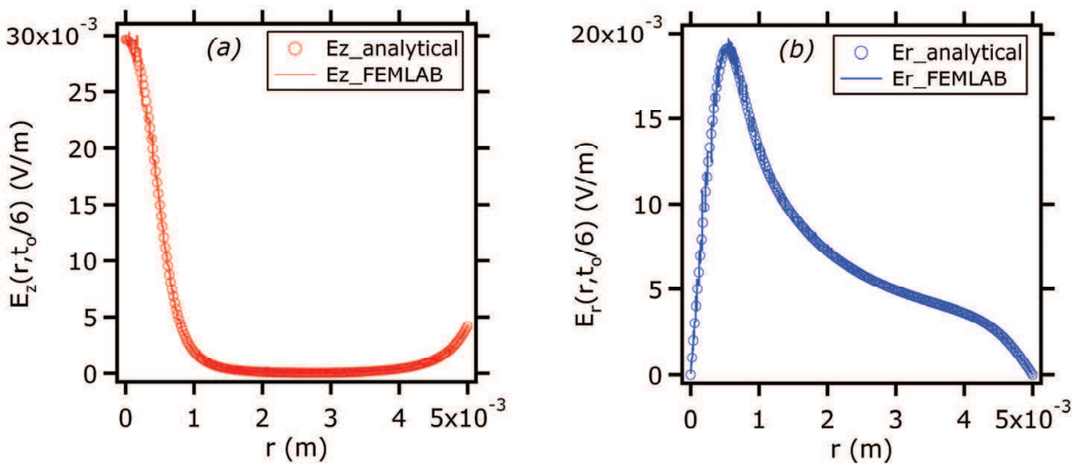

Figure 3. Plots of $E_z(r,z)\big|_{z=t_o/6}$ and $E_r(r,z)\big|_{z=t_o/6}$ versus r at 1 MHz, showing the good match between the analytical and FEMLAB solutions. The profiles correspond to the following measurement geometry: r_o=5mm, r_c=0.5mm and t_o=2mm

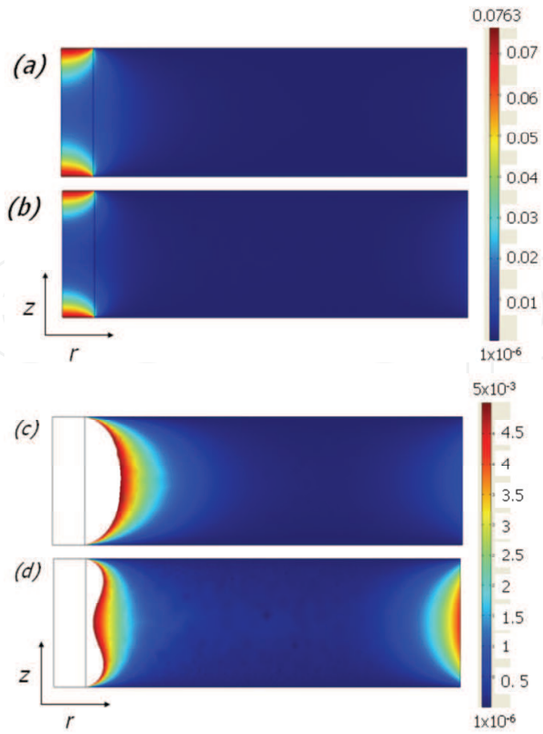

Figure 4. Surface plots of axial electric field in (V/m) emphasizing constriction behavior in (a) and (b) at frequencies of 0.1 MHz and 1 MHz respectively and skin-effect in (c) and (d) at the same two frequencies

5.2 Geometric effects on electrodynamic phenomena

Simulation studies on the effect of different geometrical parameters on the two important electrodynamic phenomena pertinent to this problem viz. the skin-effect and constriction are presented next. For these studies, the material parameters (σ,μ) and the total injected current (I_o) are left unchanged from earlier values.

Simulations for studying the skin-effect behavior (at large r) were conducted by a systematic variation of r_o and t_o at three different values of the electrode contact radius r_c. The field on the boundary, viz. $E_z(r,z)\Big|_{(r_o,\frac{t_o}{2})}$, was chosen as the representative parameter for studying the skin-effect behavior. This is because, the constriction effect is minimal at the center of the disk ($z=\frac{t_o}{2}$), whereas, the skin-effect is a maximum on the boundary ($r=r_o$).

Therefore, the field parameter $E_z(r,z)\Big|_{(r_o,\frac{t_o}{2})}$ will hereafter be referred to as the skin-effect field.

Figure 5 (a) shows the skin-effect field at 1MHz plotted versus t_o by systematically varying r_o keeping r_c constant and vice-versa. It is evident from the plots that the skin-effect field is

primarily influenced by r_o (Kelekanjeri[b] and Gerhardt 2006) and remains invariant with changes in the electrode contact radius r_c. Next, the skin-effect field goes through a maximum (at $t_o = t_{o,cri}$) before ultimately reaching a steady value. These inferences may be understood by examining the expression for the skin-effect field, which is given as:

$$E_z(r_o, \frac{t_o}{2}) = aJ_o(\kappa r_o) + \sum_m 2C'_{7m} e^{-\frac{\xi_{1m} t_o}{2}} J_o(\lambda_{1m} r_o) \tag{32}$$

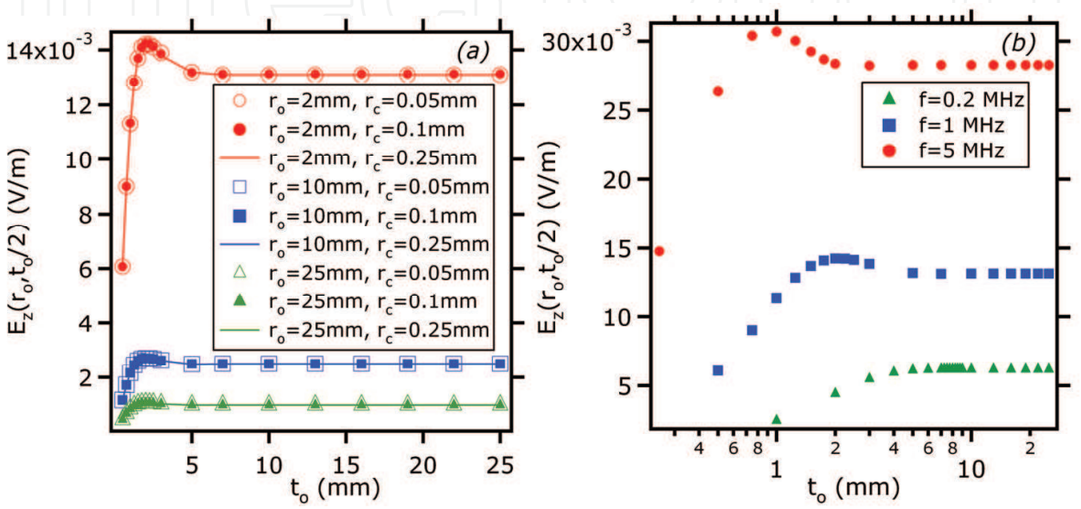

Figure 5. Plots of the skin-effect field vs. the specimen thickness t_o upon a systematic variation of (a) specimen radius r_o and electrode contact radius r_c at a frequency of 1 MHz and (b) frequency of the current by fixing r_c = 0.1mm and r_o =2mm

In general, both terms in this expression are complex quantities. The first term actually describes the skin-effect, which for the most part is dependent on a. Therefore, the magnitude of this term scales inversely with r_o, which is evident from the expression for a given earlier (see section 3.3.2). The magnitude of the second term that arises due to the constriction effect is mostly influenced by t_o. The contribution from the constriction term is significant only for small values of t_o. Therefore, the magnitude of the skin effect field is governed by both terms at small values of t_o. The maximum occurs when the phase difference between the two complex phasors is minimal. At large t_o, the contribution from the summation term becomes increasingly less significant, which is the reason for the asymptotic behavior. Physically, this implies that as the specimen thickness increases progressively, the constriction effect decays progressively to a point where it is no longer significant and the situation becomes identical to 1D skin-effect (Kelekanjeri[b] and Gerhardt 2006).

From the plot in Fig. 5(a), it is also noted that the value of $t_{o,cri}$ (corresponding to the maximum field) remains almost invariant for all combinations of r_o and r_c investigated. However, the position of the maximum ($t_{o,cri}$) was found to shift to larger values of t_o

upon decreasing the frequency, with a simultaneous drop in the skin-effect field as shown in Fig. 5(b) (Kelekanjeri[b] and Gerhardt 2006). The scaling of the field with frequency is because the parameter a is proportional to the square-root of the angular frequency. Additionally the contribution from the second term also scales with frequency and therefore the maximum is displaced further along the t_o axis upon lowering the frequency. A good analogy to this situation is that of 1D skin-effect, where the field spreads more into the conductor from the surface as the frequency decreases. In essence, frequency behaves like a kinetic parameter in controlling the dispersion of the electric field (Kelekanjeri[b] and Gerhardt 2006).

Next, the results from simulations on constriction behavior are discussed. The magnitude of the field parameter $E_z(r,z)\Big|_{(r_c,\frac{t_o}{6})}$ was chosen as the representative parameter for studying the constriction behavior (Kelekanjeri and Gerhardt 2007). The constriction effect from the previous discussion is clearly the largest at $r = r_c$, while the choice of the z co-ordinate was arbitrary. This field parameter will be referred to as the constriction field, hereon. It is intuitive that r_c should have a major impact on the constriction field, as it is in turn dependent on the impressed field, which is dictated by r_c. Therefore, the effect of systematically varying r_o and t_o on the constriction field was investigated at a fixed value of r_c =0.1mm. Figure 6(a) shows the constriction field computed at 1MHz, plotted as a function of t_o for three different values of r_o. It is clear from the plot that for a given r_o, a monotonic decrease in the constriction field is noted before ultimately reaching an asymptote. Additionally, the asymptote is noted to occur at a higher value of t_o as r_o increased. This may be understood by looking at the following expression for the constriction field $E_z(r,z)\Big|_{(r_c,\frac{t_o}{6})}$:

$$E_z(r_c,\frac{t_o}{6}) = aJ_o(\kappa r_c) + \sum_m C'_{7m}\left(e^{-\frac{\xi_{1m}t_o}{6}} + e^{-\frac{5\xi_{1m}t_o}{6}}\right)J_o(\lambda_{1m}r_c) \tag{33}$$

The contribution from the summation term decays exponentially with increasing t_o. Therefore, at small values of t_o, the magnitude of the constriction field is entirely determined by the summation term and is independent of r_o. For large values of t_o, the summation term becomes negligible and therefore the constriction field is only dependent on r_o, which explains the eventual asymptotic behavior in terms of t_o. In the intermediate regime, contributions from both terms are comparable and the extent of this regime is dependent on the parameter a, which scales inversely with r_o. Therefore, a specimen with a larger radius has an extended intermediate regime and also a smaller asymptotic constriction field, directly attributable to the contribution from the first term. The physical significance of this is that the constriction behavior equilibrates at a much smaller thickness in a specimen of smaller radius as compared to a larger one. The reason is because the field

spreads out over a larger distance in a specimen of larger radius and consequently equilibrates at a lower asymptote (Kelekanjeri and Gerhardt 2007).

Figure 6(b) shows the constriction behavior upon varying the frequency at fixed values of r_o =5mm and r_c =0.1mm. The general trend of $E_z(r,z)\Big|_{(r_c,\frac{t_o}{6})}$ vs. t_o described in the previous paragraph is also valid at all the three different frequencies investigated here. The most important effect noted upon varying the frequency is that the saturation field decreased drastically with increasing frequency, as is evident from Fig. 6(b). Additionally, the onset of saturation occurred at progressively smaller values of t_o with increasing frequency. Both these effects pertinent to the constriction region again bear testimony to the fact that frequency behaves like a kinetic parameter in determining the equilibrium field distribution, similar to that seen in Fig. 5(b) for the skin-effect field.

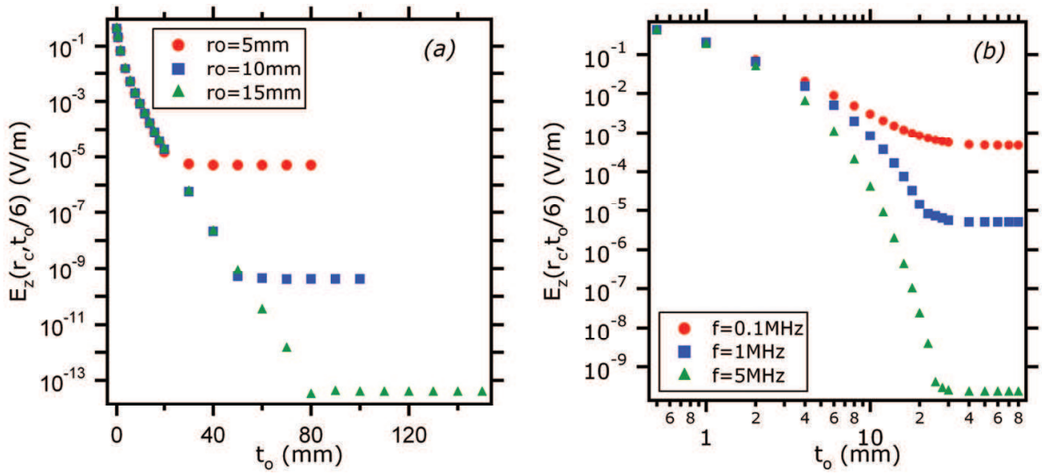

Figure 6. Plots showing the constriction field $E_z(r,z)\Big|_{(r_c,\frac{t_o}{6})}$ versus t_o with systematic variation in (a) specimen radius- r_o at a frequency of 1MHz and (b) frequency at r_o =5mm. The electrode contact radius r_c is fixed at 0.1mm for these simulations

5.3 Limiting Thickness Analysis

The concept of a limiting thickness $t_{o,lim}$, is proposed so as to investigate the applicability of the disk and semi-infinite closed-form analytical solutions to a given geometric configuration. The limiting thickness is defined as the smallest disk thickness for which a limiting field profile $E_{z,lim}\Big|_{z=\frac{t_{o,lim}}{2}}$, is reached at the center of the disk (Kelekanjeri and Gerhardt 2007). This means that a disk with thickness larger than $t_{o,lim}$, (say $t_1 > t_{o,lim}$) will yield the same profile $E_{z,lim}\Big|_{z=\frac{t_{o,lim}}{2}}$, for all values of z between $\left(\frac{t_{o,lim}}{2}\right)$ and $\left(\frac{t_1}{2}\right)$. It is

intuitive that both the limiting thickness and the limiting field profile should be frequency dependent, because the constriction effect varies with frequency as explained previously.

An optimization routine was developed for determining $t_{o,lim}$ and $E_{z,lim}\big|_{z=\frac{t_{o,lim}}{2}}$, which is described in the following. The electric field at the center of the specimen $E_z(r,z)\Big|_{(0,\frac{t_o}{2})}$ (for any arbitrary t_o), hereafter referred to as the center field, was chosen as the optimization parameter. This is because the electric field at $\left(0,\frac{t_o}{2}\right)$ was observed to be the last to equilibrate in the electric field profile at the center of the disk. The center field is given by the following expression (Kelekanjeri and Gerhardt 2007):

$$E_z(0,\frac{t_o}{2}) = a + \sum_m 2C'_{7m} e^{-\frac{\xi_{1m} t_o}{2}} \tag{34}$$

The routine begins by initializing upper and lower bounds for t_o, such that $t_{o,upper} >> t_{o,lower}$. The center fields corresponding to thickness values of $t_{o,lower}$, $t_{o,upper}$ and $t_{o,middle} = \left(\frac{t_{o,lower} + t_{o,upper}}{2}\right)$ were then determined as $E_{z,lower}$, $E_{z,upper}$ and $E_{z,middle}$ respectively. Next, the correct thickness interval ($[t_{o,lower}, t_{o,middle}]$ or $[t_{o,middle}, t_{o,upper}]$) for determination of $t_{o,lim}$ was identified by examining the relative differences between the corresponding center fields *i.e.* $\left|E_{z,upper} - E_{z,middle}\right|$ and $\left|E_{z,middle} - E_{z,lower}\right|$. The interval corresponding to the smallest difference in the fields was the obvious choice. The upper and lower bounds were updated after choosing the new interval. This procedure was repeated until convergence was achieved simultaneously in both the center field and the thickness, which uniquely determined the limiting thickness $t_{o,lim}$ and the associated limiting field profile $E_{z,lim}\big|_{z=\frac{t_{o,lim}}{2}}$, for a given geometric configuration and a frequency. The results of computations of the limiting thickness $t_{o,lim}$ and the limiting center field $E_{z,lim}\big|_{(0,\frac{t_{o,lim}}{2})}$ are listed in Table 1 for multiple frequencies. These calculations were performed for the same set of material parameters and for values of r_c and r_o of 0.5mm and 5mm respectively. It is clear from the table that the limiting thickness as well as the limiting center field, increase progressively to an asymptotic quantity with decreasing frequency.

The limiting thickness parameter thus determined was then used as a reference for comparing the disk and the semi-infinite analytical solutions with the FEMLAB solution. The FEMLAB solution proved to be indispensable in verifying the computation of $t_{o,lim}$.

Figure 7 shows the limiting electric field profile ($E_{z,lim}\big|_{z=\frac{t_{o,lim}}{2}}$ at 1 MHz) computed from the disk and the semi-infinite analytical solutions and also the FEMLAB solution for the following cases: $t_o << t_{o,lim}$, $t_o \cong t_{o,lim}$ and $t_o > t_{o,lim}$. The cross-section at the center of the disk ($z = \frac{t_o}{2}$) was chosen because, the discrepancies if present, were always a maximum here. In the case where $t_o << t_{o,lim}$, a clear mismatch is noted between the profiles yielded by the disk and the semi-infinite analytical solutions. As t_o increased, the mismatch decreased progressively and the solutions yielded a perfect match at $t_{o,lim}$ and the match remained intact for $t_o > t_{o,lim}$.

Frequency (Hz)	$t_{o,lim}$ (mm)	$E_{z,lim}\big\|_{(0,\frac{t_{o,lim}}{2})}$ (V/m)
10^6	15.4	5.08 x 10^{-6}
5x10^5	16.9	4.36 x 10^{-5}
2x10^5	19.8	2.36 x 10^{-4}
10^5	22.8	4.70 x 10^{-4}
5x10^4	22.8	6.53 x 10^{-4}
2x10^4	22.8	7.44 x 10^{-4}
10^4	22.8	7.60 x 10^{-4}
10^3	22.8	7.65 x 10^{-4}
5x10^2	22.8	7.65 x 10^{-4}

Table 1. Limiting thicknesses and limiting center fields at several frequencies via optimization of the disk solution for chosen values of r_o =5mm and r_c =0.5mm

The total number of elements used in the FEMLAB models for the cases- $t_o << t_{o,lim}$, $t_o \cong t_{o,lim}$ and $t_o > t_{o,lim}$ were 20824, 67880 and 72017 respectively. The maximum mesh size (Δ_{max}) on the vertical boundaries of the geometry (spanning a length of t_o) was adjusted so as to improve the match with the analytical solution(s). A constant value of Δ_{max} could not be used for all three cases because of memory handling constraints associated with the solver. A nearly identical profile to that of the analytical disk solution was obtained using the FEMLAB solution for $t_o < t_{o,lim}$. In cases where $t_o \geq t_{o,lim}$, the FEMLAB solution deviated marginally from the two analytical solutions, which showed a perfect match. The match could be better provided the memory constraints of the solver upon lowering Δ_{max} could be met. However, for practical purposes, the analytical disk solution and the FEMLAB

solution are in agreement with each other for all values of t_o, while, the semi-infinite analytical solution is clearly a rough approximation for $t_o << t_{o,lim}$.

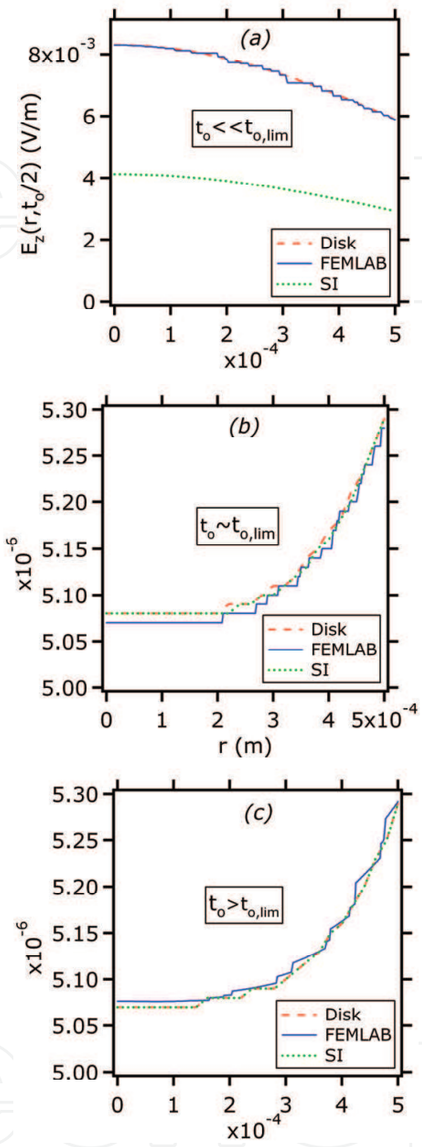

Figure 7. Plots showing the axial field at 1MHz as a function of r to show the relative match between the semi-infinite, disk analytical solutions and the FEMLAB solution for the following cases – (a) $t_o << t_{o,lim}$, (b) $t_o \cong t_{o,lim}$ and (c) $t_o \geq t_{o,lim}$

6. Computation of Specimen Impedance

In this section, a procedure for computing the complex impedance of the specimen in the shape of a cylindrical disk is described based on the expressions for the electric field distribution that were presented in section 3. As before, computation of impedance from the analytical model was validated using the FEMLAB model at a number of frequencies. The

following material properties and geometric parameters were used for computing the specimen impedance: σ=8.34 x 10^5 S/m, μ_r=1.004, r_o=6.35mm, r_c=0.5mm and t_o=2mm.
The complex impedance (Z) of a specimen for an alternating current flow situation consists of real (Z') and imaginary (Z'') components, viz. a resistance (R) and a reactance (X).

$$Z = Z' + jZ'' = R + jX \tag{35}$$

In the case of a metallic specimen, the reactance is primarily due to the contribution from the internal inductance (L_i) of the specimen. While the resistance is related directly to energy loss due to ohmic heating, the inductance describes the ability of a conductor to store magnetic energy (Hallen 1962). The expression for the complex impedance by incorporating the inductance is written as follows:

$$Z = R + j\omega L_i \tag{36}$$

The computation of R and L_i of a metallic cylindrical disk specimen using the analytical electric field expressions was conducted via energy methods (Kelekanjeri 2007). The resistance and the inductance are obtained by calculating the Joule heat-loss and the total internal magnetic energy respectively, the expressions for which, are listed as follows (Hallen 1962):

$$R = \frac{1}{I^2_{rms}} \int_V \sigma \bar{E}.\overline{E_c} dV \text{ and} \tag{37}$$

$$L_i = \frac{1}{I^2_{rms}} \int_V \bar{B}.\overline{H_c} dV = \frac{1}{I^2_{rms}} \int_V \mu \overline{H}.\overline{H_c} dV \tag{38}$$

In the above expressions $\bar{E}$ and $\overline{H}$ are the total complex electric and magnetic fields respectively, while the subscript c denotes the complex conjugate. The total magnetization- $\bar{B}$ is related to the magnetic field $\overline{H}$ by the magnetic permeability μ. The root mean square value of the current of amplitude I_o is given by $I_{rms} = \frac{I_o}{\sqrt{2}}$. The total electric field $\bar{E}$ and the magnetic field $\overline{H}$ are given in terms of the electric field components E_r and E_z as follows:

$$\bar{E} = E_r \hat{r} + E_z \hat{z} \text{ and} \tag{39}$$

$$\overline{H} = \frac{1}{j\omega\mu} \left(\frac{\partial E_z}{\partial r} - \frac{\partial E_r}{\partial z} \right) \tag{40}$$

The analytical expressions for E_r and E_z are given in section 3. The reader is referred to the Appendix for further details on evaluation of the volume integrals.
In the case of the FEMLAB model, the overall Joule heat loss and the magnetic energy are obtained by integration of the time average resistive heating per unit volume (Q_{av}) and the

magnetic energy density (W_{mav}) over the specimen volume respectively. The expressions for the time average quantities, viz. the Joule heat loss per unit volume and the magnetic energy density are given as follows (COMSOL AB[a] 2004):

$$Q_{av} = \frac{1}{2} Re\left(\vec{J}.\overline{E_c}\right) \text{ and} \tag{41}$$

$$W_{mav} = \frac{1}{4} Re\left(\overline{H}.\overline{B_c}\right) \tag{42}$$

The resistance R and the inductance L_i are subsequently obtained by dividing out the time average quantities by I_{rms}^2.

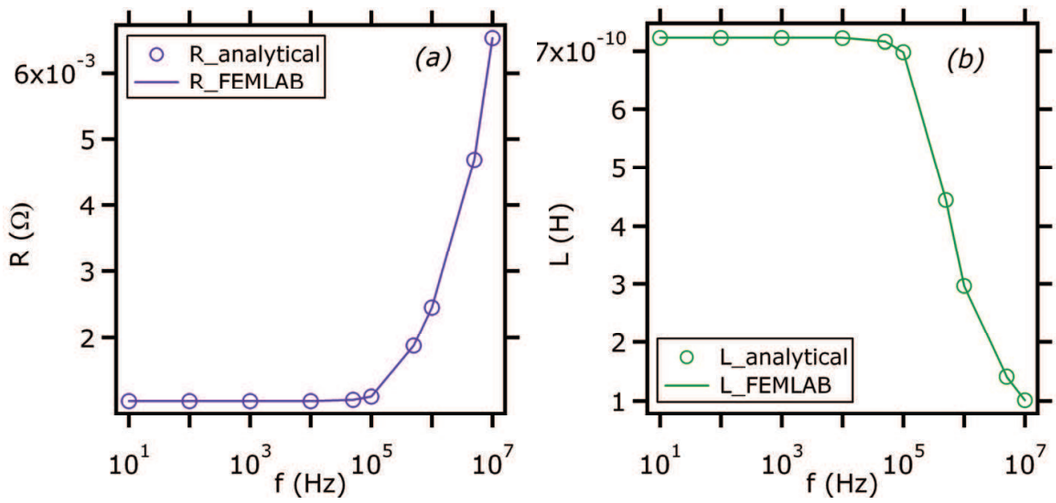

Figure 8. Plots of the frequency dependent resistance (a) and inductance (b) computed from both analytical (open symbols) and finite element models (solid line)

Plots of R and L_i as a function of the frequency are shown in Figs. 8(a) and 8(b) respectively. The perfect match between the quantities computed via the closed-form analytical solution and the finite element FEMLAB solution is evident from both plots. The resistance behavior as a function of frequency may be understood by examining the cross-section plots of $E_z(r,z)$ and $E_r(r,z)$ in Fig. 3 and the surface plots of $E_z(r,z)$ in Fig. 4. It is clear from Fig. 3(a) that the axial field $E_z(r,z)$ drops quickly to zero past the constriction region and reappears at larger values of r (near the surface). The rise in $E_z(r,z)$ near the surface (see Fig. 3(a)) is non-existent for frequencies below 10kHz. The radial field $E_r(r,z)$ (see Fig. 3(b)) on the other hand remains finite beyond the constriction region and is extended to large values of r with increase in the frequency. The extent of rise in $E_z(r,z)$ near the surface and the radial spreading in terms of $E_r(r,z)$ past the constriction region are both enhanced with increase in frequency. The variation in the field profiles for frequencies below 10kHz is negligible. This redistribution in the axial and radial fields with frequency has the effect of decreasing the Joule loss contribution from $E_z(r,z)$ and increasing that from $E_r(r,z)$

(Kelekanjeri 2007). The overall Joule heat loss however, increases drastically with frequency (10kHz and above) as the predominant effect is that of $E_r(r,z)$. Consequently, the resistance R remains relatively constant for frequencies up to 10kHz and increases progressively upon further increase in the frequency.

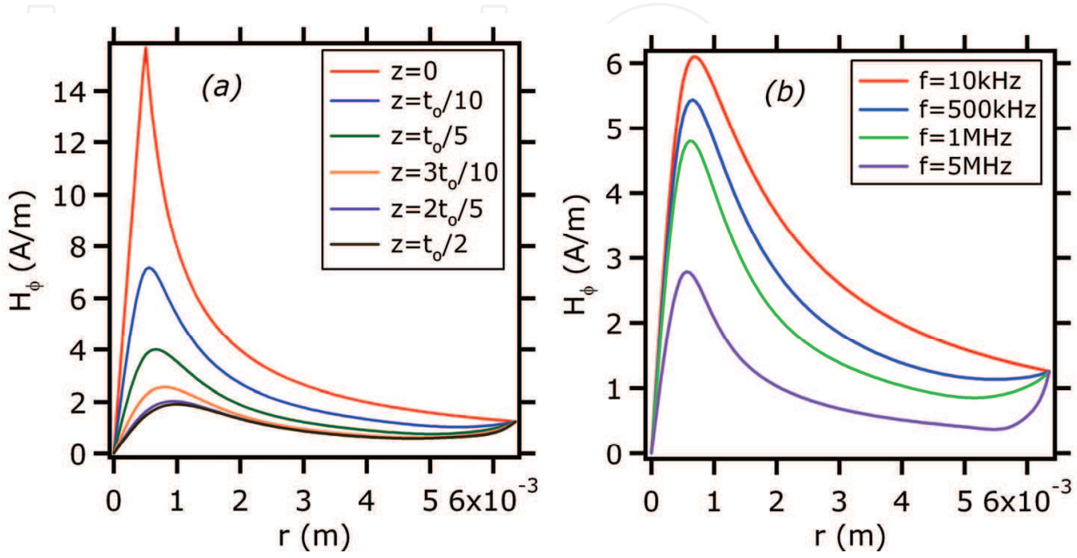

Figure 9. Plots of the magnetic field $H_\varphi(r,z)$ vs. r with varying (a) z cross-section from the surface to the center of the specimen at a frequency of 1MHz and (b) frequency at $z=\frac{t_o}{6}$. The geometry was fixed at r_o =6.35mm, r_c =0.5mm and t_o =2mm

The inductance behavior as a function of the frequency is dependent on the distribution of the magnetic field inside the specimen (Hallen 1962). Figure 9(a) shows plots of the magnetic field H_φ versus r at different z cross-sections starting from the boundary at ($z=0$) to the center of the disk ($z=\frac{t_o}{2}$). It is evident from the plots that H_φ is a maximum at $r=r_c$, (where the constriction effect is maximum) and reaches a constant value on the curved boundary ($r=r_o$). Additionally, the weakening of the magnetic field H_φ may be noted near the constriction region as z increases from 0 to $\frac{t_o}{2}$. This gradual weakening of the magnetic field is aggravated with increasing frequency, as may be seen from Fig. 9(b), which shows plots of $H_\varphi\big|_{z=\frac{t_o}{6}}$ at frequencies ranging from 10 kHz to 5 MHz. The lesser penetration of the magnetic field results in a lower overall magnetic energy for the specimen and consequently a lower internal inductance with a rise in the frequency (Hallen 1962). The reactance X on the other hand is a product of the internal inductance and the angular frequency (see equation (36)) and therefore increases with increasing frequency (Hallen 1962).

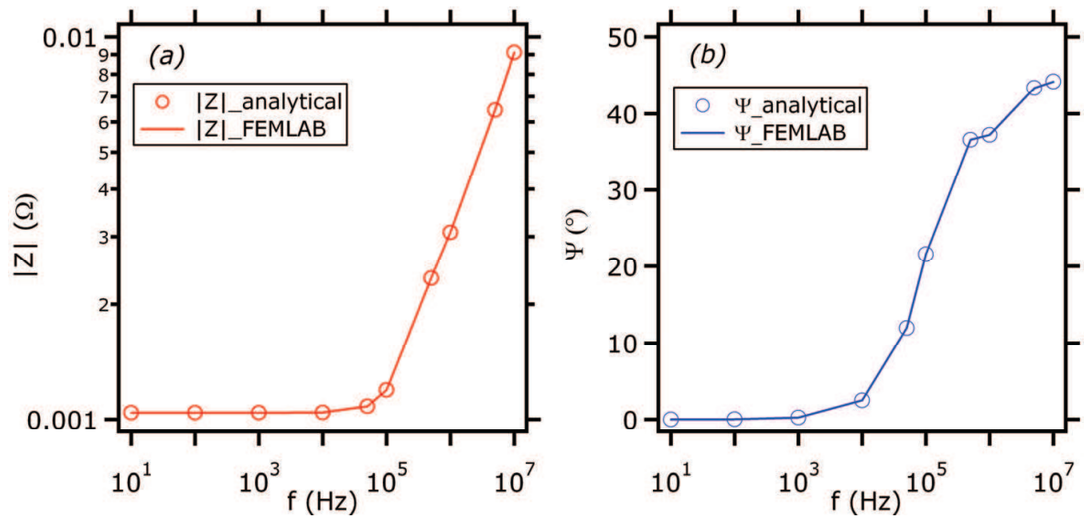

Figure 10. Plots of the complex impedance magnitude-(a) and the phase angle-(b) versus frequency showing a comparison between the analytical (open symbols) and finite element models (solid line)

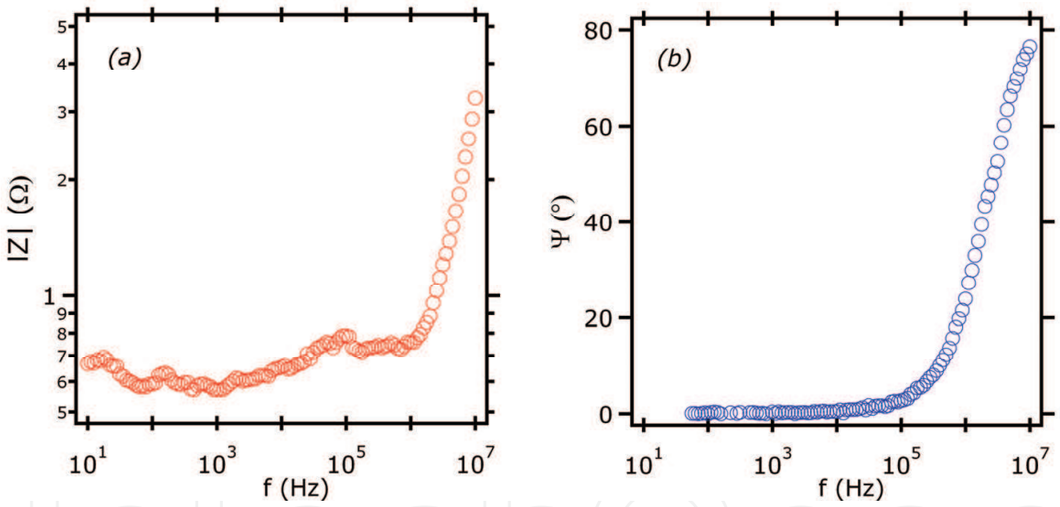

Figure 11. Plot of the complex impedance magnitude-(a) and phase angle-(b) vs. frequency from an actual two-probe impedance measurement of a superalloy specimen of dimensions- r_o =6.35mm, t_o =2mm and conductivity σ =8.34 x 10^5 S/m. The electrode contact radius r_c was 0.5mm

The magnitude of the overall impedance ($|Z| = \sqrt{R^2 + X^2}$) and the phase angle ($\psi = tan^{-1}\frac{X}{R}$) are shown as a function of the frequency in Fig. 10(a) and 10(b), for the closed-form analytical and the finite-element solutions respectively. The excellent match between the two solutions is again obvious. It is seen that the phase angle increases dramatically in the frequency range from 10kHz to 1MHz followed by a near saturation type behavior. The impedance only increases slightly from 10kHz to 100kHz, followed by a steep rise. It is interesting to note that both the resistance and reactance increase nearly at the same rate at

the highest frequencies, indicated by the saturation in ψ ~45°. The latter observation is analogous to 1-D skin-effect situation, where both components of the complex impedance increase as square root of the angular frequency at high frequencies (Gosselin, et al., 1982). It should be mentioned that the specimen impedance computed here is a function of the electrode contact radius (r_c). This is because the electric and magnetic field distribution inside the specimen is governed by the constriction effect, which in turn is affected by variations in r_c. There is however another important factor which affects the measured two-probe impedance response viz., the contact resistance between the electrode and the specimen. The present model does not account for the contact resistance effect on the overall impedance and therefore, caters to an ideal situation only.

The measured two-probe impedance and the corresponding phase angle response from a specimen with dimensions and electrical conductivity similar to that used for impedance calculations are shown in Fig. 11. It is clear that the measured impedance (Fig. 11(a)) is orders of magnitude off from the computed impedance (Fig. 10(a)); however the overall increasing trend in impedance with frequency is almost identical in shape. The measured phase angle (Fig. 11(b)) also shows a similar trend as the computed one; however, the actual magnitude of the frequency dependent phase angle is different from the computed response. The reasons for the discrepancies between the measured and computed responses are discussed below. As mentioned previously, the electrode-specimen contact resistance is one factor responsible for the rather high value of the measured impedance and is prevalent at all frequencies. Secondly, the flow of alternating current generates a time-varying magnetic field, as a consequence of Faraday's law. This magnetic field is responsible for an induced voltage besides that from the specimen, if any loops are present in the circuitry (Kelekanjeri 2007). While the contact resistance offsets the specimen impedance (at all frequencies), the induced voltage from the magnetic field primarily affects the reactance at high frequencies (10 kHz and beyond). The reactance increases nearly exponentially for frequencies above 100 kHz, owing to induced voltage from the circuitry and consequently obscures the measurement of actual impedance associated with the specimen. This is also the reason for the relatively higher values of the measured phase angle at the highest frequencies. The fluctuations in impedance noted up to 1MHz could be due to inadequate compensation of residual impedance arising from the circuitry. The problems mentioned heretofore for two-probe impedance measurements of a conducting specimen are not major concerns in the case of semiconducting or dielectric specimens due to the inherently large impedance of the specimen itself.

7. Future Work

The applicability of the present model of an ideal two-probe impedance measurement, treated as a current injection/extraction problem, is demonstrated for a fairly good conductor, in this case a nickel-base superalloy. However, the scope of this model may be extended to good semiconductors and polymer-conducting filler composites with fairly high conductivities, keeping in mind the assumptions made in the model. The validity will be ensured only when the conduction current density is still dominant over the displacement current density by orders of magnitude. As the next step, the model could be extended to address impedance measurements of more insulating materials by accounting for the displacement current term. In this case, the inherent dependence of conductivity and dielectric constant on the frequency will add more complexity into the model. This could also play a role in the case of the

conductor-filled polymer specimens, mentioned above. Another important problem in today's nanoscale research is the quantitative determination of localized electrical properties of a microstructure using scanning probe microscopy (SPM) based electrical techniques. Nanoimpedance microscopy is an SPM-based AC technique in which, a local probe tip serves as a replacement to one of the bulk electrodes for measuring the local impedance of the region of interest (Kalinin and Gruverman 2007). In this case, however, the measured response is dominated by the region that is directly underneath the probe tip, the size of which, is determined directly by the tip-radius. In addition, the contact force applied by the tip, determined by the force constant of the tip, also affects the measured response. This type of localized measurement could also be treated as a current injection/extraction problem similar to the current one. However, the spatial variations in conductivity, the surrounding medium, the relative size of the feature vs. tip-radius, the nature of the contact between the tip and the sample are all important factors that should be included in the model.

8. Summary

Closed-form analytical expressions for the electric field distribution inside a cylindrical disk conductor are presented for the problem of a two-probe impedance measurement, treated as a current injection/extraction problem. The specimen was treated as a homogeneous material medium with uniform electrical and magnetic properties. A finite element solution obtained using a commercially available finite element package, FEMLAB 3.1, was used for independent validation of the closed-form expressions. Analytical expressions for the case of an infinitely long cylinder are also given as a corollary to the disk problem.

The expressions for the axial and radial electric fields consist of terms that account for both the skin effect and the constriction effect. The skin effect term becomes important at high frequencies (10^4 Hz to 10^6 Hz) near the end regions of the disk (large r), while the constriction term is dominant in regions near the electrode contacts (small r) at all frequencies.

The effects of varying the measurement geometry viz. the electrode contact radius r_c, the disk radius r_o, and the disk thickness t_o, were investigated systematically. The skin effect behavior at high frequencies was found to be dependent only on the specimen dimensions (r_o and t_o) and was independent of the electrode contact radius r_c ($r_c << r_o$). The skin effect field reached a maximum in t_o, before eventually reaching an asymptote with increasing t_o. The dominant effect on the constriction was that of r_c. In addition, the specimen geometry also impacted the constriction behavior; the dependency on r_o was only ruled out for small values of t_o.

The concept of a limiting thickness and a limiting field profile was proposed in order to assess the range of applicability of the disk and semi-infinite analytical solutions for a given specimen geometry. Simulations indicated that the disk analytical solution and the FEMLAB solution matched with each other for all values of t_o. The semi-infinite analytical solution also matched well with the other solutions when $t_o \geq t_{o,lim}$. However, when $t_o << t_{o,lim}$, the semi-infinite solution was only a rough approximation to the actual solution yielded by the disk solution.

The real and imaginary parts of the complex impedance for an ideal two-probe impedance measurement were computed using the closed-form analytical and finite-element solutions via energy-based methods. The frequency dependent specimen resistance was found to be a

constant up to ~100kHz and increased monotonically with further rise in the frequency. The internal inductance on the other hand showed a monotonic decrease after 100kHz. These effects were explained as due to the increase in the overall Joule heat-loss and a decrease in the magnetic energy storage with rise in the frequency. The measured impedance response differed by orders of magnitude from the computed impedance due to factors such as the specimen-electrode contact resistance and the induced voltage from the measurement circuitry.

9. Acknowledgements

Research funding for this work was provided by the US Department of Energy under grant DE-FG 02-03-ER 46035. The authors would also like to acknowledge Dr. S. P. Gurrum for helpful discussions pertaining to analytical derivation and finite element models.
Figures 1(a) and (b), 2, 6(a) and 7 and Table 1 are reprinted with permission from Journal of Applied Physics 101, 0449041 Copyright American Institute of Physics (2007)

10. Appendix

I. Sifting property of the delta function

$$\int f(x)\delta(x_o - x)dx = f(x_o)$$

II. Derivative of Bessel functions

$$[x^{-\nu}J_\nu(x)]' = -x^{\nu}J_{\nu+1}(x)$$

III. Orthogonality property of Bessel functions

For a given ν, the Bessel functions $J_\nu(\lambda_{1\nu}x)$, $J_\nu(\lambda_{2\nu}x)$, $J_\nu(\lambda_{3\nu}x)$,…with $\lambda_{m\nu} = \frac{\beta_{m\nu}}{R}$ (m = *1,2,3…*) form an orthogonal basis in the interval $0 \le x \le R$ with respect to the weight function $p(x) = x$. This property is expressed as:

$$\int_0^R xJ_\nu(\lambda_{m\nu}x)J_\nu(\lambda_{n\nu}x)dx = 0 \quad (m \neq n)$$

$$= \frac{R^2}{2}J^2{}_{\nu+1}(\lambda_{m\nu}R) \quad (m = n)$$

IV. Indefinite integral of product of Bessel functions

$$\int_z \left\{(k^2 - l^2)t - \frac{(\mu^2 - \nu^2)}{t}\right\} J_\mu(kt)J_\nu(lt)dt$$

$$= z\left\{kJ_{\mu+1}(kz)J_\nu(lz) - lJ_\mu(kz)J_{\nu+1}(lz)\right\} - (\mu - \nu)J_\mu(kz)J_\nu(lz)$$

V. Complex identities

If u and v are any two complex numbers, then the following identities hold true for operations on their complex conjugates $\overline{u}$ and $\overline{v}$.

a. (a) $\overline{(u \pm v)} = \overline{u} \pm \overline{v}$

b. (b) $\overline{(uv)} = \bar{u}\bar{v}$

c. (c) $\overline{J_\mu(u)} = J_\mu(\bar{u})$, where $J_\mu(x)$ is a Bessel function in x of order μ.

11. References

Abramowitz, M. & Stegun, I. A. (1964) eds. *Online Version of Handbook of Mathematical Functions*, U. S. Government Printing Office, Washington

Bauerle, J. E. (1969) Study of solid electrolyte polarization by a complex admittance method. *Journal of the Physics and Chemistry of Solids,* 30, (Dec. 1969) (2657-70), ISSN: 0022-3697.

Bowler[a,] N. a. (2004). Analytical solution for the electric field in a half space conductor due to alternating current injected at the surface. *Journal of Applied Physics*, 95, 1, (1st January, 2004) (344-348), DOI: 10.1063/1.1630700

Bowler[b,] N. a. (2004). Electric field due to alternating current injected at the surface of a metal plate. *Journal of Applied Physics*, 96, 8, (15th October, 2004) (4607-4613), DOI: 10.1063/1.1793332

Casimir, H. B. G. & Ubbink, J. (1967). The skin effect, I. Introduction; the current distribution for various configurations. *Philips Technical Review*, 28, 9, (271-283),

COMSOL AB[a] (2004). *User's Guide to Electromagnetics Module, FEMLAB 3.1* COMSOL AB, Stockholm, Sweden

COMSOL AB[b] (2004). *FEMLAB 3.1 User's Guide*, COMSOL AB, Stockholm, Sweden

Costache, G. I. & Ney, M. M. (1988). A time domain approach for determining ground impedance on printed circuit boards.*2nd Symposium on Antenna Technology and Applied Electromagnetics*, pp. 1-6, ISBN: 0969256310, Winnipeg, Canada, August 10-12, 1988

Cottingham, W. N. & Greenwood, D. A. (1991). *Electricity and Magnetism* Cambridge University Press, ISBN: 0-521-36803-0, New York

Gerhardt, R. A. (2005). Impedance Spectroscopy and Mobility Spectra, In: *Encyclopedia of Condensed Matter Physics* eds. Bassani, G., Liedl, G. & Wyder, P., (350-363), Elsevier Press, ISBN-13: 978-0-12-227610-1, New York, NY, USA

Giacoletto, L. J. (1996). Frequency- and Time-Domain Analysis of Skin Effects. *IEEE Transactions on Magnetics*, 32, 1, (220-229), Publisher Item Identifier: S 0018-9464(96)00089-I

Gosselin, J. R., Rochon, P. & Gauthier, N. (1982). Study of eddy currents in a cylindrical wire: an undergraduate laboratory experiment. *American Journal of Physics*, 50, 5, (May 1982) (440-443)

Gray, A. & Mathews, G. B. (1952). *A Treatise on Bessel Functions and Their Applications to Physics*, Macmillan and Co., Limited, 2nd edition edited by Gray, A. and MacRobert, T. M., London

Hallen, E. G. (1962). *Electromagnetic Theory, Translated from the Swedish ed. by Runar Gasstrom*, Wiley & Sons Inc., New York

Kalinin, S. & Gruverman, A. (2007). *Scanning probe microscopy: Electrical and electromechanical phenomena at the nanoscale*, Springer, 1st, ISBN: 978-0-387-28667-9, New York, NY, USA

Kelekanjeri[a], V. S. K. G. & Gerhardt, R. A. (2006). Characterization of microstructural fluctuations in Waspaloy exposed to 760°C for times up to 2500 h. *Electrochimica Acta*, 51, (1873-1880), DOI:10.1016/j.electacta.2005.02.099

Kelekanjeri[b], V. S. K. G. & Gerhardt, R. A. (2006). Finite-element Validation of Electric Field Distribution inside a Cylindrical Conductor for an Ideal Two-Probe Impedance Measurement.*COMSOL 2006 Users Conference*, pp. 117-123, 0-9766792-2-1, Boston, MA, USA, October 22nd-24th, COMSOL Inc., USA

Kelekanjeri, V. S. K. G. & Gerhardt, R. A. (2007). Electric field distribution within a metallic cylindrical specimen for the case of an ideal two-probe impedance measurement. *Journal of Applied Physics*, 101, (0449041-04490410), DOI: 10.1063/1.2405734

Kelekanjeri, V. S. K. G. (2007). *Non-destructive Electrical Characterization of Controlled Waspaloy Microstructures, Ph.D. Dissertation*, Materials Science and Engineering, Georgia Institute of Technology, Atlanta

Kreyszig, E. (1994). *Advanced Engineering Mathematics* Wiley Eastern Limited, 5th, ISBN: 81-224-0016-7, New Delhi, India

Ney, M. M. (1991). Striction and Skin Effects on the Internal Impedance Value of Flat Conductors. *IEEE Transactions on Electromagnetic Compatibility*, 33, 4, (321-327), IEEE Log Number 9102196

Weber, H. J. & Arfken, G. B. (2004). *Essential Mathematical Methods for Physicists* Elsevier, ISBN: 81-8147-616-6, New Delhi

www.mathworld.com

Zou, X., Makram, T. & Gerhardt, R. A. (2002). Detection of compositional fluctuations in high temperature exposed Waspaloy.*Electrically Based Microstructural Characterization III. Materials Research Society Symposium*, pp. 301-306, 1 55899 635 4, Boston, MA, USA, Materials Research Society

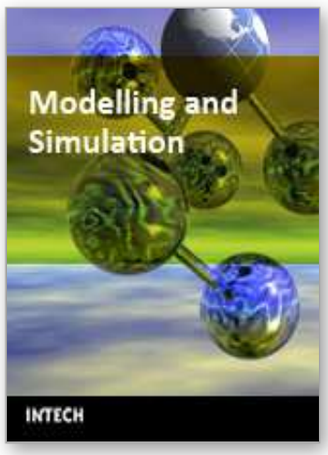

Modelling and Simulation

Edited by Giuseppe Petrone and Giuliano Cammarata

ISBN 978-3-902613-25-7
Hard cover, 688 pages
Publisher I-Tech Education and Publishing
Published online 01, June, 2008
Published in print edition June, 2008

This book collects original and innovative research studies concerning modeling and simulation of physical systems in a very wide range of applications, encompassing micro-electro-mechanical systems, measurement instrumentations, catalytic reactors, biomechanical applications, biological and chemical sensors, magnetosensitive materials, silicon photonic devices, electronic devices, optical fibers, electro-microfluidic systems, composite materials, fuel cells, indoor air-conditioning systems, active magnetic levitation systems and more. Some of the most recent numerical techniques, as well as some of the software among the most accurate and sophisticated in treating complex systems, are applied in order to exhaustively contribute in knowledge advances.

InTech Europe
University Campus STeP Ri
Slavka Krautzeka 83/A
51000 Rijeka, Croatia
Phone: +385 (51) 770 447
Fax: +385 (51) 686 166
www.intechopen.com

InTech China
Unit 405, Office Block, Hotel Equatorial Shanghai
No.65, Yan An Road (West), Shanghai, 200040, China
中国上海市延安西路65号上海国际贵都大饭店办公楼405单元
Phone: +86-21-62489820
Fax: +86-21-62489821

IntechOpen